

## Supporting Information

### **Dendrite-free lithium-metal battery at high rate realized by composite solid electrolyte with ester-PO<sub>4</sub> complex and stable interphase**

Zhaoshuai Zhang,<sup>1</sup> Long Zhang,<sup>1\*</sup> Yanyan Liu,<sup>1</sup> Tingting Yang,<sup>1</sup> Zhiwen Wang,<sup>1</sup>

Xinlin Yan,<sup>2</sup> Chuang Yu<sup>3</sup>

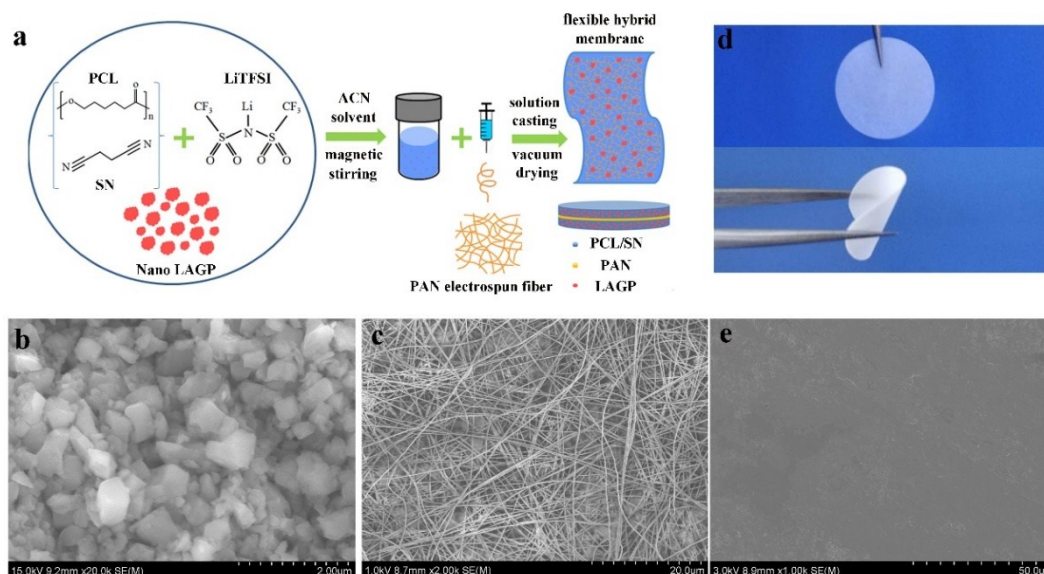
<sup>1</sup>Clean Nano Energy Center, State Key Laboratory of Metastable Materials Science  
and Technology, Yanshan University, Qinhuangdao, Hebei 066004, China

<sup>2</sup>Institute of Solid State Physics, Vienna University of Technology, Wiedner Hauptstr.  
8-10, 1040 Vienna, Austria

<sup>3</sup>Department of Mechanical and Materials Engineering, University of Western Ontario,  
1151 Richmond St, London, Ontario, N6A 3K7, Canada

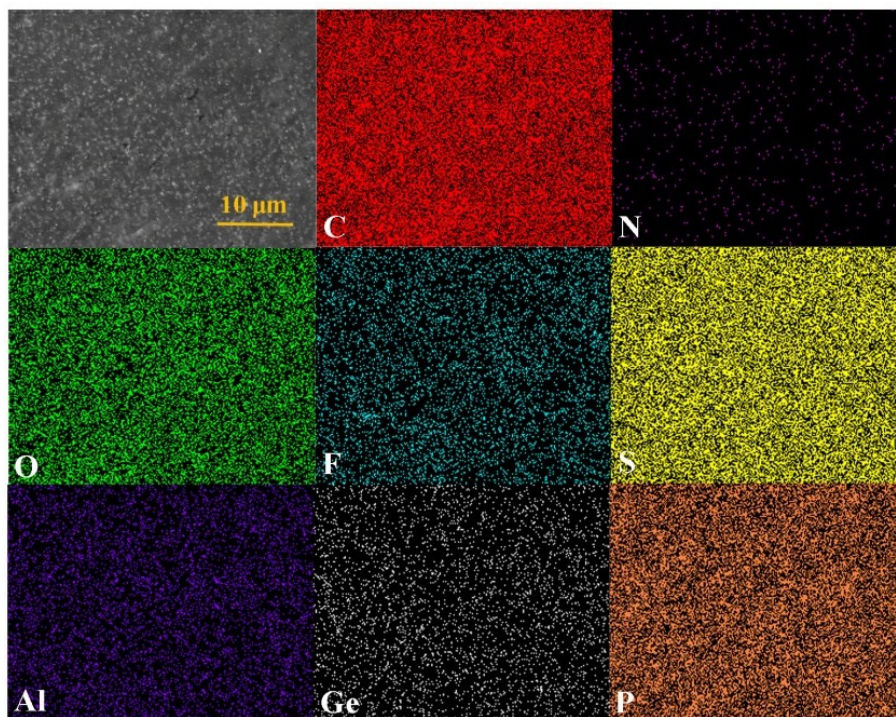
\* Corresponding author Email: lzhang@ysu.edu.cn

Figure S1a depicts the schematic illustration of the preparation process of PCL-SN-PAN-LAGP (PSPL) composite electrolyte membrane. The facile process contains major steps including: 1) dispersing LAGP in a PCL/SN/LiTFSI dissolved ACN solution, 2) casting the suspension onto a PAN skeleton, and 3) vacuum drying to solidify the sandwich-structured PSPL polymer composite membrane with the PAN electrospun fiber as skeleton. Figures S1b and c show the SEM images of LAGP particles within a size range of 200–800 nm and the PAN skeleton consisting of uniformly distributed PAN nanofibers. Observed from optical photographs (Figure 1d) and SEM images (Figure 1e), the as-prepared composite membrane exhibits excellent flexibility and a smooth and homogenous surface with a dense microstructure.



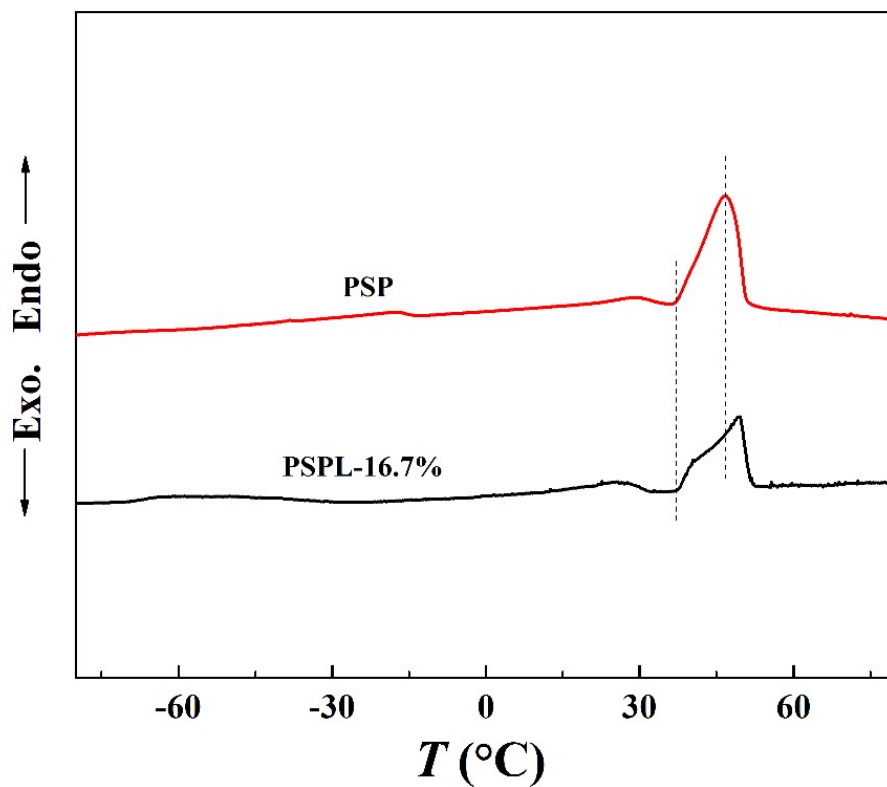
**Figure S1.** (a) Schematic illustration for the preparation of the sandwiched polymer composite membrane. Typical SEM images of the LAGP powders (b), the PAN-electrospun fibers (c), and the solidified composite membrane (e). (d) Optical photographs of the flexible composite membrane.

Figure S2 shows the EDS mapping of C, N, O, F, S, Al, Ge, and P elements in PSPL-16.7% polymer composite membrane. It can be clearly seen the uniform elemental distribution in the membrane. The bright points in the SEM image are LAGP particles.



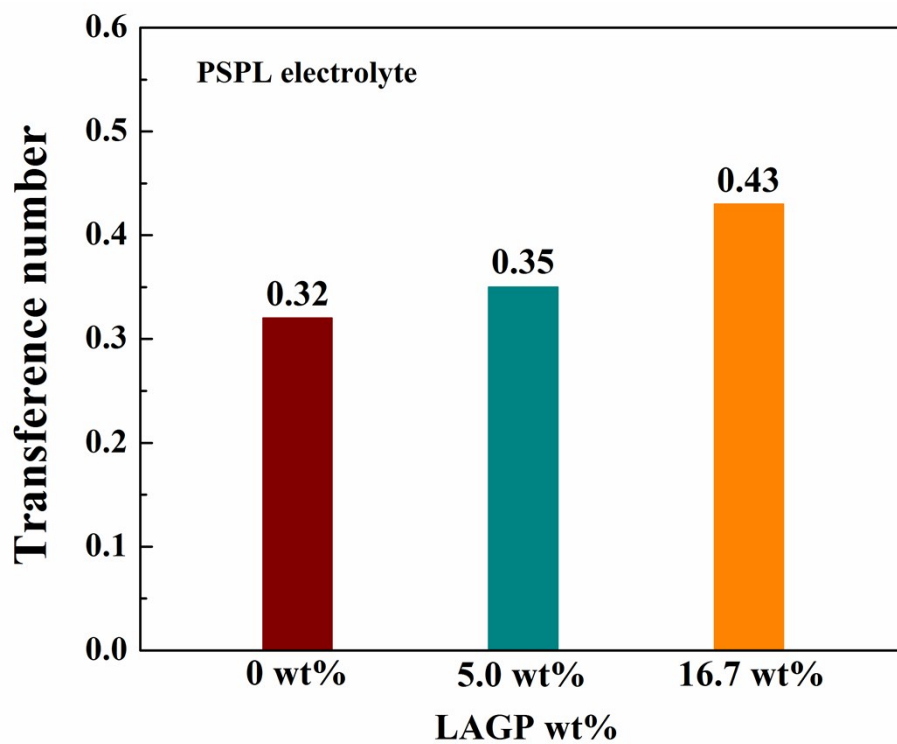
**Figure S2.** SEM image of PSPL-16.7% composite membrane (a) and the corresponding EDS mapping of C, N, O, F, S, Al, Ge, and P elements.

Figure S3 shows the DSC profiles of PSP and PSPL-16.7%. Compared the PSP sample without LAGP, the incorporation of LAGP in PSPL-16.7% does not significantly affect the melting point and the crystallization.



**Figure S3.** DSC curves of PSP and PSPL-16.7%.

Figure S4 shows that Li ion transference number ( $t_{Li^+}$ ) increases with increasing LAGP concentration. The PSPL-16.7% hybrid composite electrolyte possesses the highest  $t_{Li^+}$  with a value of 0.43, much higher than the LAGP-free PSP sample.

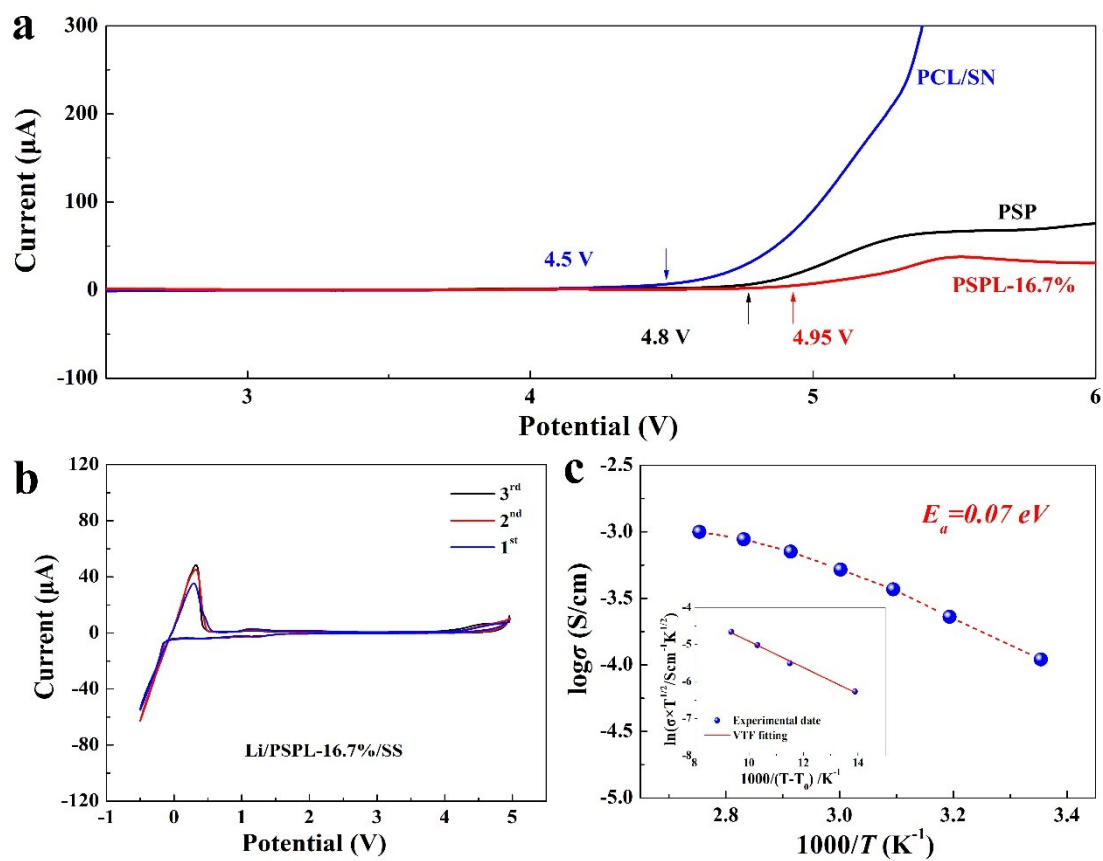


**Figure S4.** Li<sup>+</sup> transference numbers of PSP, PSPL-5% and PSPL-16.7% solid electrolytes.

Figure S5a shows the linear scanning voltammetry curves for different electrolytes. The tests were performed on asymmetric cells with a stainless-steel sheet as the working electrode and a lithium foil as the counter/reference electrode. The onset of the current response of PSPL-16.7% is obviously suppressed by adding LAGP. The voltage window is over 4.5 V and is obviously higher than those of PSP (without LAGP) and PCL/SN (without LAGP or skeleton). The wide electrochemical window is favorable for the composite solid electrolyte matched with high-potential cathodes. The cyclic voltage (CV) measurement of PSPL-16.7% electrolyte was performed in a voltage range of 0.5-5 V, as shown in Figure S5b. There is no side reaction except lithium deposition and dissolution near 0 V. The second and third circles of the CV curve are almost overlapping and reflect higher current values than the first circle, indicating that PSPL-16.7% has good cycling stability and forming an interphase with reduced resistance. This result further confirms that PSPL-16.7% electrolyte membrane has a wide electrochemical stability window.

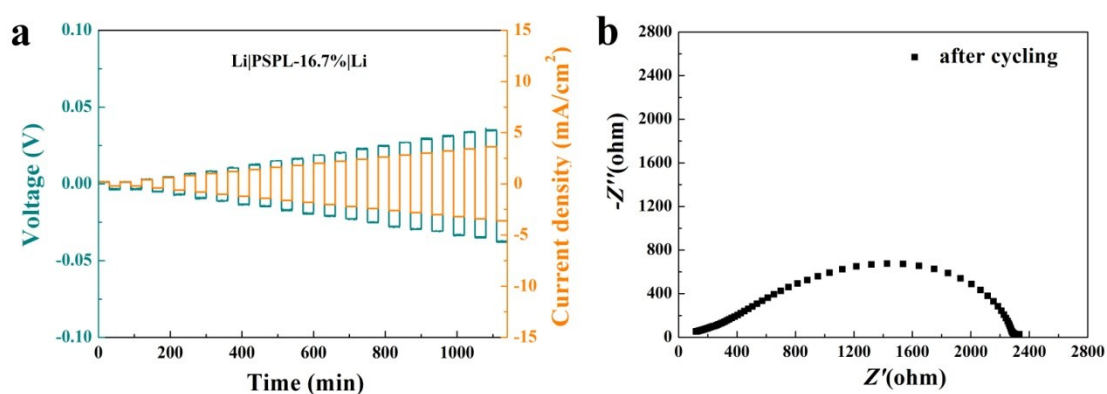
The temperature dependence of the ionic conductivity of the PSPL-16.7% composite membrane is presented in Figure S5c. It can be seen that the slope of the curve in the lower temperature region (25 to 50 °C) is slightly different from that in the higher temperature region (50 to 100 °C). This difference is caused by the softening of PCL at 50 °C. This result verifies that the composite electrolyte can well work at high temperature without short circuits. As shown in the inset of Figure 5c, the activation energy  $E_a$  of the  $\text{Li}^+$  conduction was determined by fitting the Arrhenius graph with the Vogel–Tamman–Fulcher (VTF) empirical equation in terms of the coupling

between ions and polymer chains dynamics. The activation energy of PSPL-16.7% composite membrane was calculated to be  $E_a=0.07$  eV, a reasonable value in polymer composite electrolytes



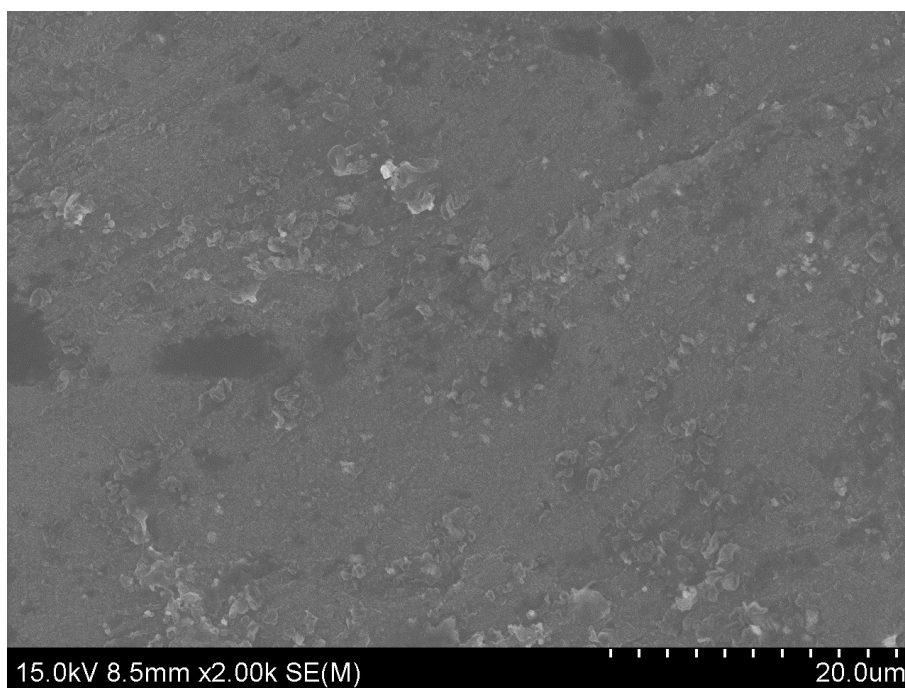
**Figure S5.** (a) Linear sweep voltammetry curves of PCL/SN, PSP, and PSPL-16.7%. (b) CV curves of PSPL-16.7% at a scan rate of 1 mV/s. (c) The Arrhenius conductivity plot of PSPL-16.7% from 25 to 90 °C.

Figure S6 shows the galvanostatic intermittent cycling of the Li/PSPL-16.7%/Li symmetric cell at step-increased current densities at room temperature ( $\sim 20\text{ }^{\circ}\text{C}$ ). The PSPL-16.7% hybrid polymer composite electrolyte is able to withstand a current density more than  $3.6\text{ mA/cm}^2$  without short circuit or sudden voltage increase during the Li plating/stripping cycling.



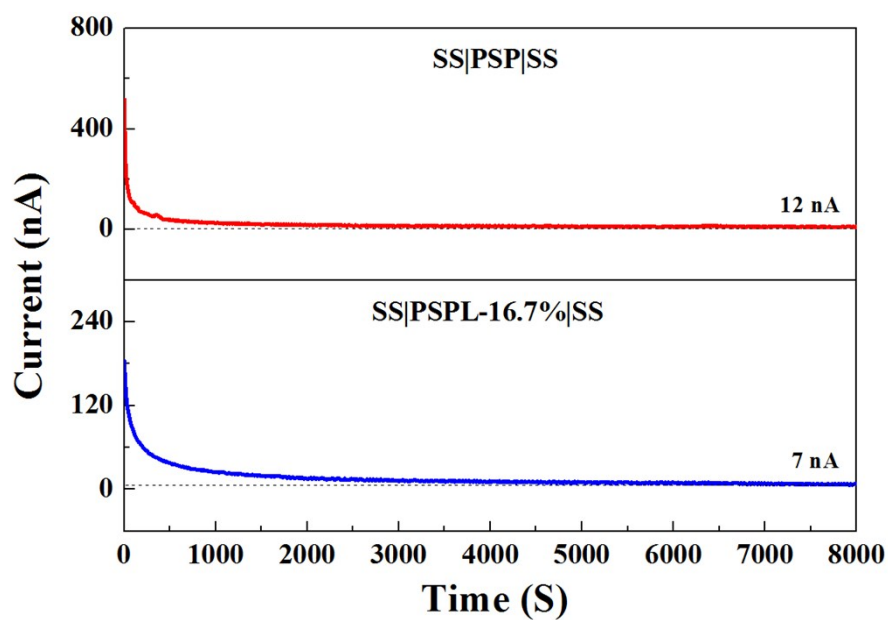
**Figure S6.** (a) Galvanostatic intermittent cycling of the Li/PSPL-16.7%/Li symmetric cell at step-increased current densities at room temperature ( $\sim 20\text{ }^{\circ}\text{C}$ ). (b) The impedance spectrum of the Li/PSPL-16.7%/Li symmetric cell after cycling.

Figure S7 shows the SEM morphology image of the Li surface in contact with the composite electrolyte after the long-term galvanostatic polarization test on the Li/PSPL-16.7%/Li cell. No uneven aggregation or protrusion of lithium is observed. This also verifies a stable interface at Li anode.



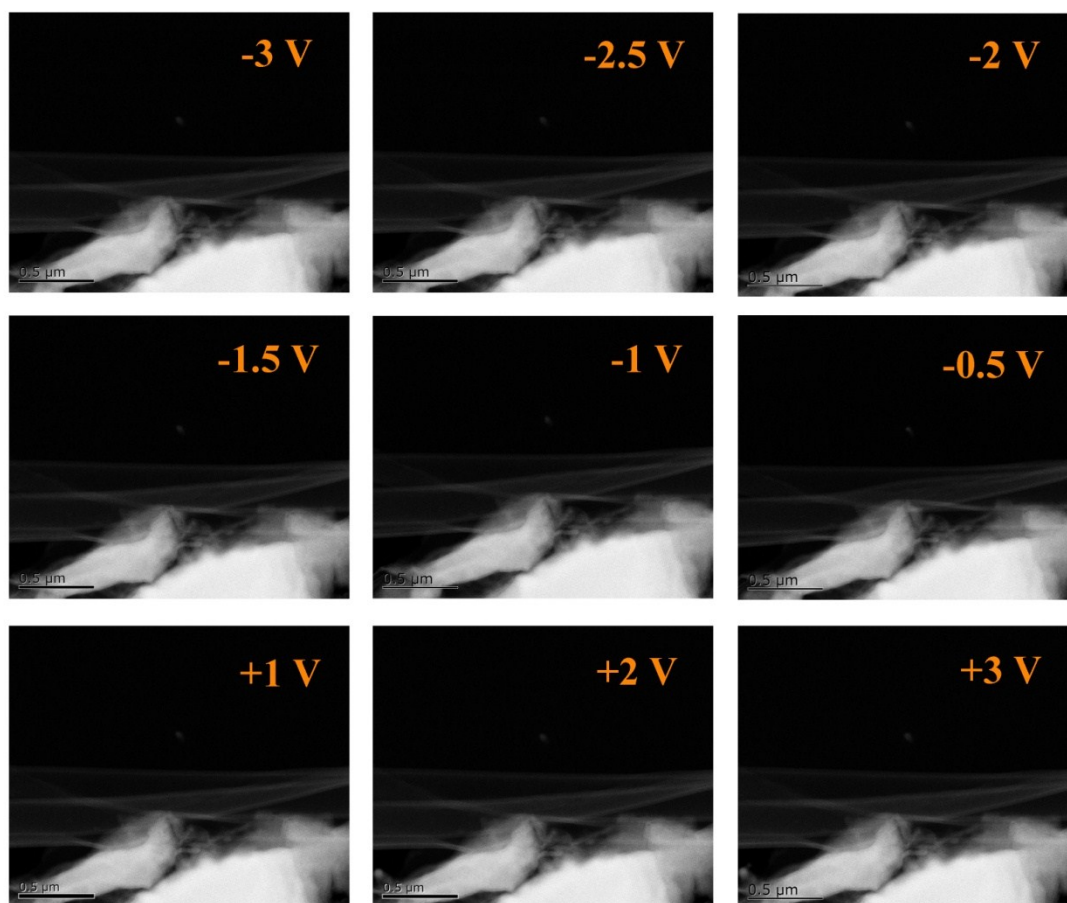
**Figure S7.** Morphology of metallic Li electrode at the side facing the electrolyte after galvanostatic cycling of Li/PSPL-16.7%/Li symmetric cell.

Figure S8 shows the DC polarization tests for PSP and PSPL-16.7% with stainless steel as blocking electrodes. The electronic conductivity of the PSPL-16.7% composite electrolyte is calculated to be  $3.8 \times 10^{-10}$  S/cm, half of the PSP value.



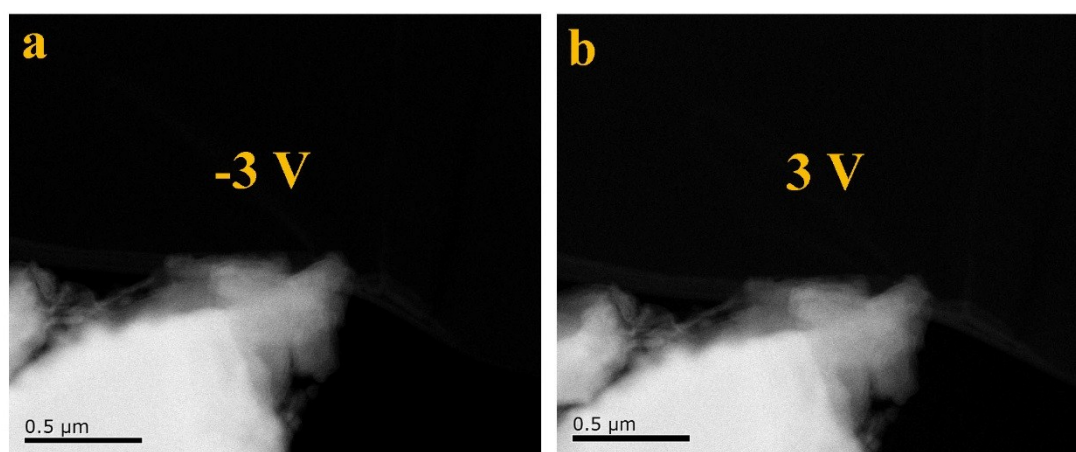
**Figure S8.** DC polarization current as a function of time for PSP and PSPL-16.7% with stainless steel as blocking electrodes.

Figure S9 shows the TEM-ADF images of a Cu/PSPL-16.7%/Li cell potentiostatic cycled at different voltages. No uneven Li deposition or Li dendrite is observed.



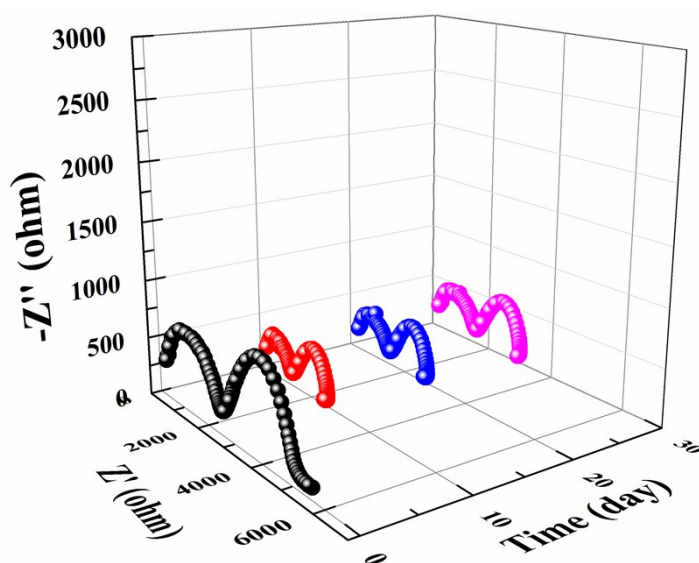
**Figure S9.** *In situ* TEM-ADF images for potentiostatic cycling of a Cu/PSPL-16.7%/Li cell at different voltages.

Figure S10 shows the *in situ* TEM-ADF images of potentiostatic cycling in the voltage range of 3 V to -3V on another Cu/PSPL-16.7%/Li cell for a reproducible test. Again, no uneven Li deposition or Li dendrite is observed. This result demonstrates the excellent compatibility and stability of the hybrid composite electrolyte against lithium metal.



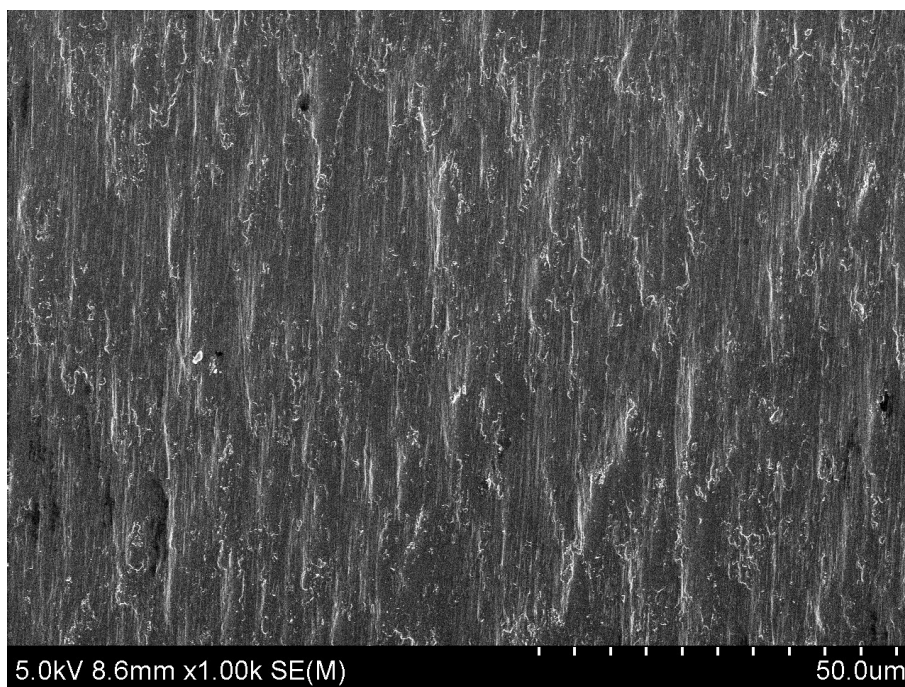
**Figure S10.** *In situ* TEM-ADF images of potentiostatic cycling in the voltage range of 3 V to -3V in another Cu/PSPL-16.7%/Li cell for a reproducible test.

Figure S11 shows the AC impedance diagrams of Li/PSPL-16.7%/Li symmetric cell at different aging times, so as to test the chemical stability of the polymer composite electrolyte with lithium metal. The semicircle at the real axis at high frequency can be attributed to the bulk and grain boundary resistances, and the middle and low frequency semicircles is induced by the interfacial impedance between the PSPL-16.7% electrolyte and Li. The interface resistance decreases and then keeps relatively stable after aging. This indicates the formation of a stable interphase layer with low resistance at the polymer/Li interface, verifying the superior chemical stability between the polymer composite electrolyte and Li.



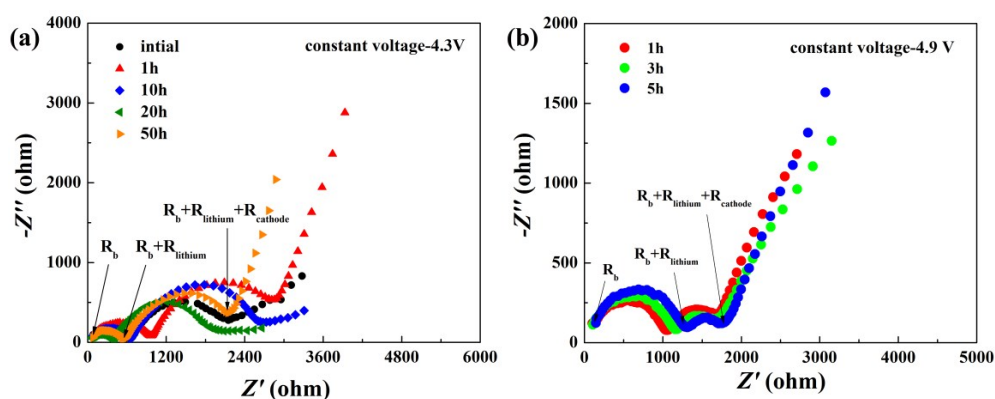
**Figure S11.** AC impedance spectra of Li/PSPL-16.7%/Li cell for different aging times.

Figure S12 show the SEM morphology image of the pristine Cu foil before Li deposition.



**Figure S12.** SEM morphology image of the pristine Cu foil.

To evaluate the stability of the electrolyte against the cathode materials, the constant voltage charging tests on  $\text{LiFePO}_4/\text{PSPL-16.7\%/Li}$  and  $\text{LiNi}_{0.5}\text{Mn}_{1.5}\text{O}_4/\text{PSPL-16.7\%/Li}$  all-solid-state batteries were performed, as shown in Figure S13. The impedance spectra contain high frequency phase resistance ( $R_b$ ), electrolyte/Li interfacial resistance ( $R_{\text{lithium}}$ ), and electrolyte/cathode interfacial resistance ( $R_{\text{cathode}}$ ). The resistance changes during the constant voltage charging are relatively small, indicating a limited degradation/decomposition at the positive electrode/electrolyte interface.



**Figure S13.** Impedance variation of  $\text{LiFePO}_4/\text{PSPL-16.7\%/Li}$  (a) and  $\text{LiNi}_{0.5}\text{Mn}_{1.5}\text{O}_4/\text{PSPL-16.7\%/Li}$  (b) all-solid-state batteries charging for different times at constant voltages of 4.3 and 4.9 V, respectively.

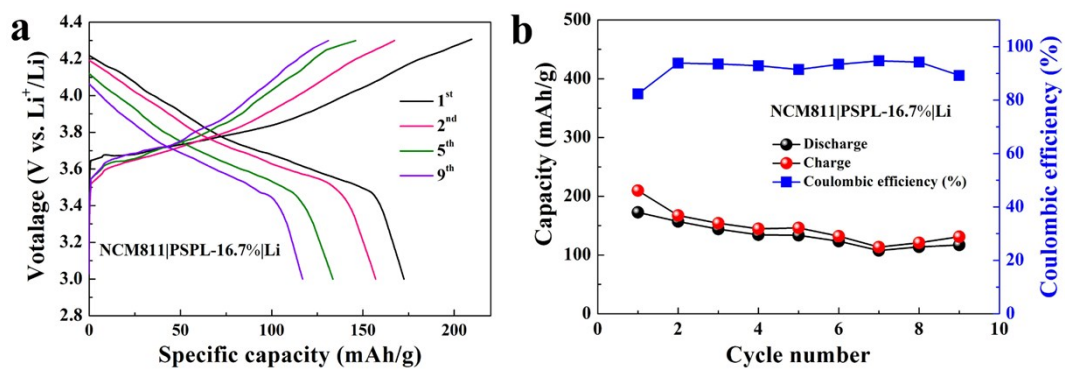


**Figure S14.** Typical charge/discharge curves (a) and cycling performance (b) of the  $\text{LiNi}_{0.8}\text{Co}_{0.1}\text{Mn}_{0.1}\text{O}_2/\text{PSPL-16.7\%}/\text{Li}$  battery at a current density of 0.1 C at 50 °C.

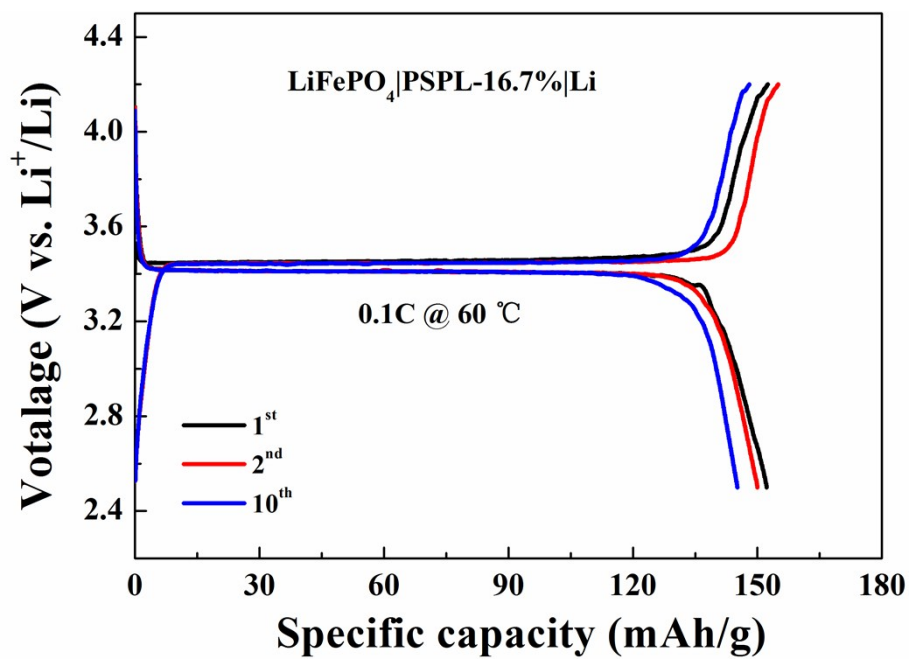


**Figure S15.** Typical charge/discharge curves of the LiFePO<sub>4</sub>/PSPL-16.7%/Li battery at a current density of 0.1 C at 60 °C.

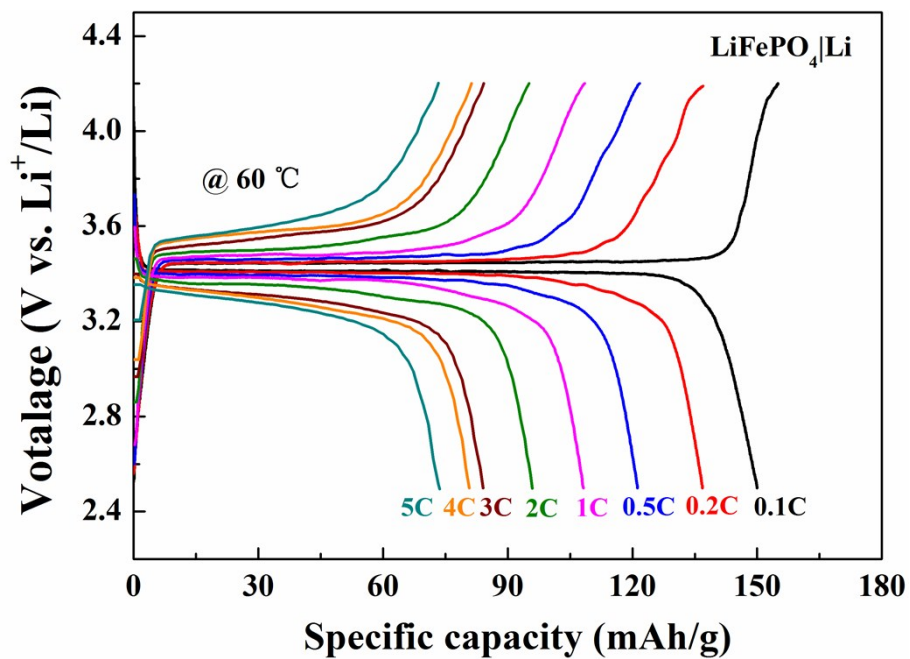


**Figure S16.** Charge-discharge profiles of the LiFePO<sub>4</sub>/PSPL-16.7%/Li battery at various current rates at 60 °C.

**Table S1.** The ionic conductivity ( $\sigma$ ) of the polymer composite electrolytes for different components.

	<b>PCL</b>	<b>PEO</b>	<b>LAGP</b>	<b>LiTFSI</b>	<b>SN</b>	<b>PAN</b>	<b><math>\sigma</math>, S/cm</b>
PG	√		√				$<10^{-7}$
PLG	√		√	√			$5 \times 10^{-5}$
PCL/SN	√			√	√		$>1 \times 10^{-4}$
PSP	√			√	√	√	$1.5 \times 10^{-4}$
PSL	√		√	√	√		$>3 \times 10^{-4}$
PSPL	√		√	√	√	√	$>3 \times 10^{-4}$
PLL		√	√	√			$1 \times 10^{-4}$

**Table S2.** Ionic conductivity and cycling performance of the Li/Li symmetric cell with PSPL-16.7% hybrid polymer composite electrolyte compared with those with selected LAGP-based polymer composite electrolytes from literature.

	Components	$\sigma$ , (mS/cm)	Current density	Cycles (h)	Note*
			(mA/cm <sup>2</sup> )		
1	PEO-LAGP	0.167	0.3	200	Ref. [1]
2	PEO-LAGP	0.09	0.05	400	Ref. [2]
3	PEO-LPOS-LAGP	0.8	0.1	1200	Ref. [3]
4	PVDF-HFP-LAGP	0.92	0.2	400	Ref. [4]
5	PEO-LATP/PAN	0.65	0.3	400	Ref. [5]
6	PPC-PEO-LAGP	0.016	0.1	100	Ref. [6]
7	PSPL-16.7%	0.68	1~4	650	This work

**\*Refs.**

- [1] X. Wang, H. Zhai, B. Qie, Q. Cheng, A. Li, J. Borovilas, B. Xu, C. Shi, T. Jin, X. Liao, Y. Li, X. He, S. Du, Y. Fu, M. Dontigny, K. Zaghbi and Y. Yang, *Nano Energy*, 2019, **60**, 205-212.
- [2] G. Hou, X. Ma, Q. Sun, Q. Ai, X. Xu, L. Chen, D. Li, J. Chen, H. Zhong, Y. Li, Z. Xu, P. Si, J. Feng, L. Zhang, F. Ding and L. Ci, *ACS Appl. Mater. Interfaces*, 2018, **10**, 18610-18618.
- [3] Z. Zhang, Y. Zhao, S. Chen, D. Xie, P. Cui and X. Xu, *J. Mater. Chem. A*, 2017, **5**, 16984–16993
- [4] Q. Guo, Y. Han, H. Wang, S. Xiong, Y. Li, S. Liu and K. Xie, *ACS Appl. Mater. Interfaces*, 2017, **9**, 41837-41844.
- [5] D. Li, L. Chen, T. Wang and L. Z. Fan, *ACS Appl. Mater. Interfaces*, 2018, **10**, 7069-7078.
- [6] Z. Wang, H. Gu, Z. Wei, J. Wang, X. Yao and S. Chen, *Ionics*, 2019, **25**, 907-916.